Three-dimensional noninvasive imaging of the vasculature in the mouse brain using a high resolution photoacoustic scanner

Jan Laufer,[1] Edward Zhang,[1] Gennadij Raivich,[1,2] and Paul Beard[1,*]

[1]Department of Medical Physics and Bioengineering, University College London, Gower Street, London WC1E 6BT, UK

[2]Centre for Perinatal Brain Research, University College, Gower Street, London WC1E 6BT, UK

*Corresponding author: pbeard@medphys.ucl.ac.uk

Received 6 October 2008; revised 13 January 2009; accepted 16 January 2009; posted 22 January 2009 (Doc. ID 102329); published 30 March 2009

The application of a novel photoacoustic imaging instrument based on a Fabry–Perot polymer film sensing interferometer to imaging the small animal brain is described. This approach provides a convenient backward mode sensing configuration that offers the prospect of overcoming the limitations of existing piezoelectric based detection schemes for small animal brain imaging. Noninvasive images of the vasculature in the mouse brain were obtained at different wavelengths between 590 and 889 nm, showing that the cerebral vascular anatomy can be visualized with high contrast and spatial resolution to depths up to 3.7 mm. It is considered that the instrument has a role to play in characterizing small animal models of human disease and injury processes such as stroke, epilepsy, and traumatic brain injury.

OCIS codes: 170.5120, 170.0110, 170.3880.

1. Introduction

Small animal models are widely used as a research platform to study basic brain function and disease and injury processes in an effort to improve the diagnosis and treatment of neurological conditions such as stroke, traumatic brain injury, and epilepsy [1]. There is a consequent need to characterize these models not only by revealing anatomical changes but also by eliciting precursive functional information via the physiological and metabolic status of tissue. Imaging techniques such as x-ray CT, MRI, SPET, and PET have all been used for small animal neuroimaging. However, these modalities either provide solely anatomical information (CT) or functional information with relatively low spatial resolution (SPET/PET), or where they do provide both tend to be limited in the range of physiological parameters, and thus the specificity of the functional information, they can provide [2,3]. Optical imaging techniques can provide a wide variety of functional parameters by exploiting changes in absorption, scattering, or fluorescence [3,4]. For example, by using absorption spectroscopy, it is possible to monitor changes in oxyhemoglobin and deoxyheomoglobin and cytochrome oxidase, all of which are important markers of brain function [5]. Furthermore there is a wide range of optical contrast agents available that can be targeted to specific biomolecules to reveal processes at a cellular or molecular level [6]. However, strong scattering in most tissues limits penetration depth and spatial resolution. Thus, techniques such as optical coherence tomography and confocal and multiphoton microscopy that rely on predominantly unscattered or singly backscattered light to provide spatial information are unable to provide penetration depths exceeding ~1 mm [4]. This limits small animal optical brain imaging to visualizing the surface of the cortex, and even then, to achieve the highest possible

0003-6935/09/10D299-08$15.00/0

resolution, it is usually necessary to expose the cortex by removing the scalp and thinning or resecting the skull [3]. Diffuse optical tomography can achieve penetration depths of several centimeters using near infrared (NIR) light but has found limited application in small animal brain imaging on account of its relatively low spatial resolution [7].

Photoacoustic imaging offers an alternative approach that provides the spectroscopic based specificity and functional capability of optical imaging methods but without the attendant penetration depth/spatial resolutions limitations. The technique involves irradiating the tissue surface with nanosecond NIR or visible laser pulses. Absorption of the laser energy and subsequent thermoelastic expansion produces broadband pulses of ultrasound that propagate to the surface where they are detected at different spatial locations. By measuring the time of arrival of the acoustic pulses at each location, and knowing the speed of sound in tissue, the acoustic signals can be backprojected to reconstruct a 3D image of the absorbed optical energy distribution. Thus, while image contrast is based on tissue optical properties, principally absorption, spatial resolution is defined by the physics of ultrasound propagation. The fundamental spatial resolution limit is set by the frequency dependent acoustic attenuation of soft tissues and scales with penetration depth: for centimeter depths, submillimeter spatial resolution is possible, decreasing to sub-100 μm for millimeter penetration depths and sub-10 μm spatial resolution for depths of a few hundred micrometers. For depths beyond 1 mm or so, photoacoustic imaging therefore provides significantly higher spatial resolution than purely optical imaging methods—a consequence of the much lower scattering that ultrasound waves undergo in soft tissues compared to photons. Although, hard tissues such as bone strongly scatter ultrasound, the skull of mice or rats, unlike larger animals such as primates or indeed humans, is usually sufficiently thin that this does not excessively compromise image quality.

The most important source of endogenous photoacoustic image contrast is hemoglobin due to its strong optical absorption at visible and NIR wavelengths. This makes photoacoustic imaging particularly well suited to visualizing the vasculature. In addition, quantitative functional information can be potentially obtained via measurements of absolute blood oxygen saturation and flow—the former by obtaining images at multiple wavelengths and applying a spectroscopic analysis to exploit the differences in the spectral characteristics of oxyhemoglobin and deoxyhemoglobin [8], the latter by extracting the acoustic Doppler shift encoded onto photoacoustic signals emitted by moving red blood cells [9,10]. In common with other optical imaging techniques there is the further prospect of using targeted exogenous contrast agents to image specific cellular, intracellular, and molecular receptors [11,12]. This ability to noninvasively image vascular anatomy and function, as well as provide molecular information over the spatial scales of the mouse or rat brain, suggests photoacoustic imaging could be a powerful investigative tool for studying small animal cerebral hemodynamics, oxygenation, and cellular function. For example, the ability to localize deficiencies in tissue perfusion and oxygenation status, as well as any ensuing neuronal cell damage, would be of major benefit in the study of stroke and other conditions where hypoxic ischemic damage occurs.

Several experimental studies have now demonstrated the ability of photoacoustic imaging to noninvasively image the structure and function of the vasculature in the rat or mouse brain with a spatial resolution in the tens to hundreds of micrometers range [13–20]. The most commonly used implementation employs a circular scanning detection geometry. In this approach, a piezoelectric ultrasound detector or array of detectors is mechanically scanned around the circumference of the head of the animal while the surface is illuminated with pulses of laser light. This method provides the necessarily large angular detection aperture for high quality image reconstruction and allows the excitation light to be delivered without it being obscured by the detector. The disadvantage, however, lies in coupling the ultrasound to the detector: either the animal has to be fitted with a breathing mask [13,17,19] and completely immersed in water or some other acoustic couplant or only the top of the head is acoustically coupled via a thin walled helmet to a water bath containing the ultrasound receiver [14–16]. Neither is particularly convenient in terms of animal handling and achieving the correct orientation of the head with respect to the detection system. It would be significantly more convenient to map the photoacoustic signals over the illuminated top surface of the head: the so-called backward or reflection mode of detection. The challenge then is to deliver the laser light without it being obstructed by the detectors. One approach is to deliver the light circumferentially around a mechanically scanned focused piezoelectric detector, so-called photoacoustic microscopy [21]. Although high quality images of the superficial cortical vasculature in a mouse have been obtained with this method [22], the highest lateral spatial resolution is achieved only at a limited range of depths, those that coincide with the nondivergent region of the transducer focus. It also remains to be seen whether this sequential scanning approach can be parallelized to overcome the inevitable limited acquisition speed associated with mechanical scanning.

In this paper we describe the use of a novel high resolution photoacoustic scanner for small animal brain imaging that can overcome these limitations. The distinguishing feature of the system is that it employs an optical ultrasound imaging sensor based on a Fabry–Perot polymer film interferometer (FPI) that is transparent. The sensor can therefore be

placed on the surface of the animal head, the excitation laser pulses transmitted through it, and the photoacoustic signals mapped in 2D over the irradiated region. In this way it provides a truly backward mode planar detection configuration that does not require the animal to be wholly immersed in acoustic couplant and avoids the handling difficulties associated with the use of a helmet that cylindrical detection schemes require. Since a tomographic image reconstruction approach is employed it does not suffer from the depth limited spatial resolution limitations of using a fixed focus transducer, and the sensor read-out scheme can be readily parallelized to achieve high frame rates.

The design, operating principles, and performance of the scanner are described in Ref. [23]. This study showed that the system could provide high fidelity 3D images of tissue mimicking phantoms. In this paper, the emphasis is on applying the instrument to imaging the mouse brain. Section 2 provides a brief overview of the operation of the scanner and its performance; Section 3 presents images of the vascular anatomy in the mouse brain obtained at a variety of excitation wavelengths.

2. Photoacoustic Imaging System

A. Principles of Operation

A full description of the imaging system is described in Ref. [23]. Briefly, it comprises a tunable pulsed excitation laser system that is used to generate the photoacoustic waves and a 2D planar backward mode optical ultrasound mapping system for recording them over the surface of the skin. From the measured photoacoustic signals, a 3D image is then reconstructed.

The excitation laser system is a fiber coupled type I optical parametric oscillator (OPO) (GWU VisIR) pumped by the 355 nm frequency tripled output of a Q-switched Nd:YAG laser (Spectra-Physics, Quanta Ray LAB170). This system is capable of providing 8 ns optical pulses over the wavelength range from 410 to 2100 nm with end-of-fiber pulse energies in the 12–36 mJ range (depending on wavelength) at a pulse repetition frequency of 10 Hz.

The key component of the ultrasound mapping system is a sensor head that is placed in light contact with the surface of the mouse head over the region indicated by the dotted line in the photograph in Fig. 1. A drop of water is sandwiched between the sensor head and the skin surface in order to acoustically couple the photoacoustic signals to the sensor. The critical requirement in this respect is that there is no air between the sensor and the skin, as this would act as a strong acoustic reflector and impede the transmission of the acoustic waves. The sensor head comprises a 10 mm thick wedged poly(methyl methacrylate) substrate with a polymer film FPI formed on its lower side. The FPI is fabricated by vacuum depositing a multilayer structure consisting of a 38 μm thick Parylene C polymer film spacer

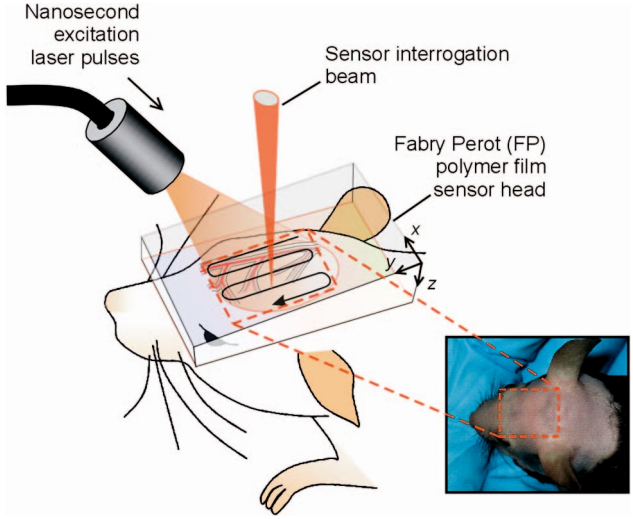

Fig. 1. (Color online) Experimental arrangement. The FP sensor head is placed on the surface of the mouse head over the region indicated on the photograph. Nanosecond excitation laser pulses emitted by a tunable OPO laser system are directed on to the sensor head, and transmitted through it into the underlying tissue thereby exciting acoustic waves. A second laser emitting at 1550 nm provides a focused interrogation laser beam that is raster scanned over the surface of the sensor in order to map the distribution of the photoacoustic waves arriving at the sensor head. From the 2D distribution of the photoacoustic waves, a 3D image is then reconstructed.

sandwiched between a pair of dichroic dielectric mirrors. These mirrors are highly reflective (>95%) between 1500 and 1650 nm but highly transmissive between 600 and 1200 nm. Excitation laser pulses in the latter wavelength range can therefore be transmitted through the sensor head into the underlying tissue. Absorption of the laser energy produces photoacoustic pulses that travel back to the sensor head where they modulate the optical thickness of the FPI and hence its reflectivity.

The sensor is read out by raster scanning a focused interrogation laser beam (at 1550 nm where the FPI mirrors are highly reflective) point-by-point over the surface of the sensor using an $x-y$ galvanometer based scanner. At each point of the scan, the sensor is optimally biased by tuning the interrogation laser wavelength to the point of maximum slope on the interferometer transfer function, the relationship between reflected optical power and phase. Under these conditions, a small acoustically induced modulation of the optical thickness of the FPI can be regarded as being linearly converted, via the interferometer transfer function, to a corresponding reflected optical power modulation. This time-varying optical power modulation, which represents the photoacoustic waveform, is then detected by an InGas photodiode-transimpedance amplifier unit and recorded using a digital storage oscilloscope (DSO). Once a waveform has been acquired at a particular spatial point on the sensor it is stored within the onboard memory of the DSO. The interrogation laser

beam is then moved to the next scan point and the process repeated. At the end of the 2D scan, the entire set of waveforms are downloaded from the DSO to a PC and input to a k-space backpropagation algorithm [24] in order to reconstruct a 3D image of the initial pressure distribution $p_o(x,y,z)$: the photoacoustic image.

B. System Performance

The maximum area over which the interrogation laser beam can be scanned over the sensor is defined by a circle of diameter 50 mm. The $1/e^2$ diameter of the laser beam at its focus is 64 μm and represents, to a first approximation, the dimensions of the acoustically sensitive region of the sensor. The minimum scan step size (limited by the 12 bit resolution of the PC digital-to-analog conversion card that controls the optical scanner) is 10 μm. The peak noise-equivalent pressure of the sensor is approximately 0.2 kPa over a measurement bandwidth of 20 MHz—comparable to that of a 1 mm diameter polyvinylidine fluoride piezoelectric receiver. The frequency response of the sensor is defined primarily by the acoustic thickness of the polymer film spacer [23] and is characterized by a smooth roll-off from a maximum value at 100 kHz (the –3 dB cutoff frequency of the ac-coupled photodiode) to zero at 100 MHz with a –3 dB bandwidth of 22.2 MHz. A plot of the frequency response of the sensor can be found in Ref. [23].

The point-to-point acquisition time of the system described in Ref. [23] was approximately 1 s per scan step. This was limited by the sequential nature of the waveform downloading process in which each photoacoustic waveform was downloaded to the PC via a GPIB interface immediately following its acquisition. In the current study, a different acquisition approach was adopted whereby the complete set of waveforms acquired over the scan were stored within the onboard memory of the DSO and downloaded to the PC in a single step. Although this enabled the point-to-point acquisition time of the scanner itself to be reduced to 10 ms [25], the average acquisition time achieved in this study was limited by the 10 Hz pulse repetition frequency of the laser system to 100 ms per scan step.

To obtain a measure of the spatial resolution that the system can provide, measurements of the instrument line spread function (LSF) have been made and are reported in Ref. [23]. The lateral LSF depends on the overall detection aperture (the scan area), the effective acoustic element size, spatial sampling interval, and the bandwidth of the sensor. Furthermore it depends on the angular aperture subtended by the detection aperture and therefore the axial and lateral position of the source. Taking into account the relatively small scan areas ($\sim$1 cm^2) used in this study, the data presented in Ref. [23] suggest a lateral LSF in the range from 50 to 100 μm for depths up to 5.5 mm at the center of the detection aperture. Unlike the lateral LSF, the vertical LSF is, to a first approximation, spatially invariant and dependent largely on the bandwidth, which is defined by the thickness of the polymer film spacer. Again, using the measurements obtained in Ref. [23], the vertical LSF is estimated at approximately 50 μm. In both cases the estimated LSFs are measures of the instrument response alone. They do not account for frequency dependent acoustic attenuation and should therefore be regarded as only approximate indicators of the spatial resolution that will be in achieved when imaging tissue.

3. Noninvasive Imaging of the Mouse Brain

Ex vivo images of the cerebral vasculature of 3 month old mice (CL57/BL6) were obtained. The time between sacrifice and image acquisition was approximately 90 min. The images were acquired at a variety of excitation wavelengths in order to identify which might be optimal in terms of image contrast and penetration depth. Three experiments were undertaken. In the first, an excitation wavelength of 590 nm was used because it is strongly absorbed by hemoglobin and so offered the prospect of achieving high contrast. However it was expected to provide a relatively small penetration depth due to its absorption by blood in the capillary bed and thus is likely to be best suited to visualizing superficial vessels. For this reason, the use of longer wavelengths was explored. In the second experiment two wavelengths, 637 and 800 nm, were used. Both wavelengths are attenuated less than 590 nm, and combining the two meant that a higher total fluence could be obtained for increased penetration depth. Finally, in the third experiment an excitation wavelength of 889 nm was used.

All the images were obtained noninvasively through the intact skin and skull, the only preparation being that the hair around the region of interest was removed using VEET hair removal cream. In all cases, no signal averaging was used and the incident laser fluence was below the safe maximum permissible exposure (MPE) for skin [26]. To aid the visualization of deeply lying features, a depth dependent scaling factor was used to compensate for optical and acoustic attenuation in a manner analogous to time-gain compensation used in diagnostic medical ultrasound imaging. The scaling factor was obtained empirically from the 3D reconstructed data $p_o(x,y,z)$ set by extracting the maximum value of p_o from each $x-y$ plane in the data set as a function of z to give $p_{o(m)}(z)$. An exponential function of the form $e^{-\alpha z}$ was then fitted to $p_{o(m)}(z)$ by varying α, and it is this function that was used to compensate for attenuation in the reconstructed image. Apart from this and the use of an interpolation algorithm, no other image processing was employed. The reconstructed images in this paper are presented as maximum intensity projections or volume rendered representations. The latter are also available as animated volume rendered images and can be viewed online as Media 1, Media 2, Media 3 or the University College

London website [27]. These animations provide the most compelling demonstrations of the 3D imaging capability of the system.

A. λ=590 nm

In the first experiment, the excitation laser wavelength was set to 590 nm. The incident fluence was 6.8 mJ/cm^2 and thus significantly below the MPE of 20 mJ/cm^2 for skin at this wavelength. The sensor interrogation beam was scanned over an area of dimensions 9 mm × 10 mm in steps of 100 μm, and a single photoacoustic waveform was acquired at each step. The total number of waveform acquisitions was therefore 9000, and the time taken to acquire these was 15 min. A 3D image data set of dimensions 9 mm × 10 mm × 3.8 mm was then reconstructed from the detected signals using the k-space backpropagation algorithm referred to in Subsection 2.A. Lateral ($x-y$) and vertical ($y-z$) maximum intensity projections (MIP) were computed from the 3D reconstructed data set and are shown in Fig. 2. From these images, the principal cerebral cortical vessels, the sagittal sinus, transverse sinus, and other superficial veins can be identified. At 590 nm, penetration depth is relatively low due to strong optical absorption by blood in the capillary bed. As a consequence only vessels on the surface of the cortex are evident. Note that the $y-z$ MIP shows only the vasculature on the cortical surface around the side of the head, not vessels extending vertically into the underlying white matter. This can be seen more clearly in the animated volume rendered representation available online (Media 1) from which a sequence of four stills at different angles is shown in Fig. 3.

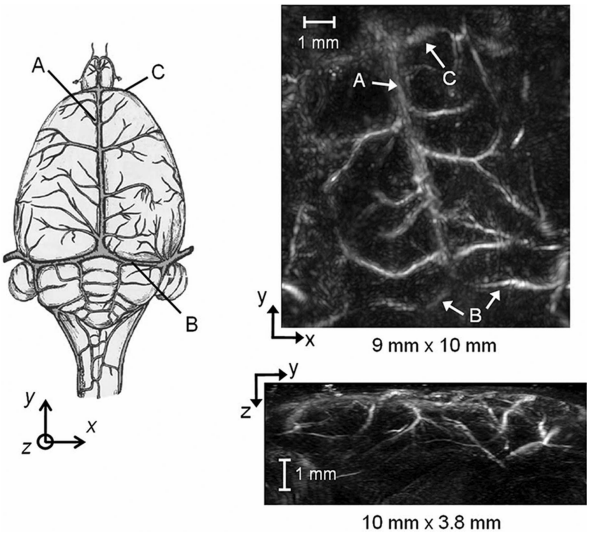

Fig. 2. Photoacoustic image of the vasculature in the mouse brain obtained using an excitation wavelength of 590 nm. Left, schematic of superficial cerebral vascular anatomy: A, superior sagittal sinus; B, transverse sinus; C, inferior cerebral vein. Top right, $x-y$ maximum intensity projection (MIP) of 3D photoacoustic image; bottom right, $y-z$ MIP.

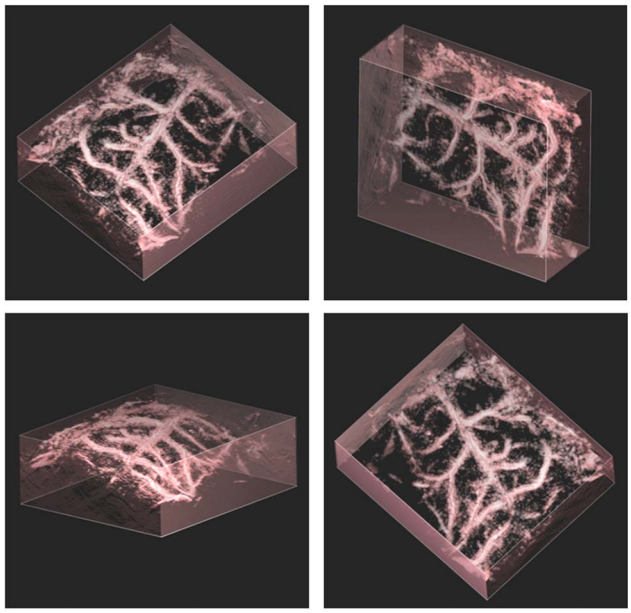

Fig. 3. (Color online) Volume rendered representation of images of the mouse brain vasculature at different viewing angles obtained using an excitation wavelength of 590 nm (Media 1). This image was reconstructed from the data set used to form the MIPs shown in Fig. 2.

B. λ=637 and 800 nm

A second experiment was undertaken using the same mouse. This time, however, the OPO signal and idler beams at 637 and 800 nm, respectively, were combined to provide a single excitation beam at these two wavelengths. The incident fluence was therefore higher than in the previous example at 10 mJ/cm^2 but still below the MPE. The spatial scan parameters and acquisition time were the same as the previous experiment. Figure 4 shows the lateral and vertical MIPs. Figure 5 (Media 2) shows four stills from the animated volume rendered representation available online. The superficial cerebral vessels are again evident on the $x-y$ MIP. In addition, absorption by the retina has produced features corresponding to the location of the eyes. However, unlike the image obtained at 590 nm (Fig. 3), the penetration depth is significantly greater due to the reduced optical absorption of blood at 637 and 800 nm and the higher fluence. The most apparent features, which are not visible in the image obtained at 590 nm, are the sinus rectus and inferior sagittal sinus. The latter can be seen to extend deep into the brain to a depth of approximately 3.1 mm Again this is most apparent in the online animated volume rendered representation.

C. λ=889 nm

A third experiment was undertaken using a different mouse and a wavelength of 889 nm. To ensure that the whole of the cortical vasculature could be imaged, the photoacoustic signals were recorded over a larger area (12 mm × 14 mm) than in the previous experiments. This required reducing the step size to

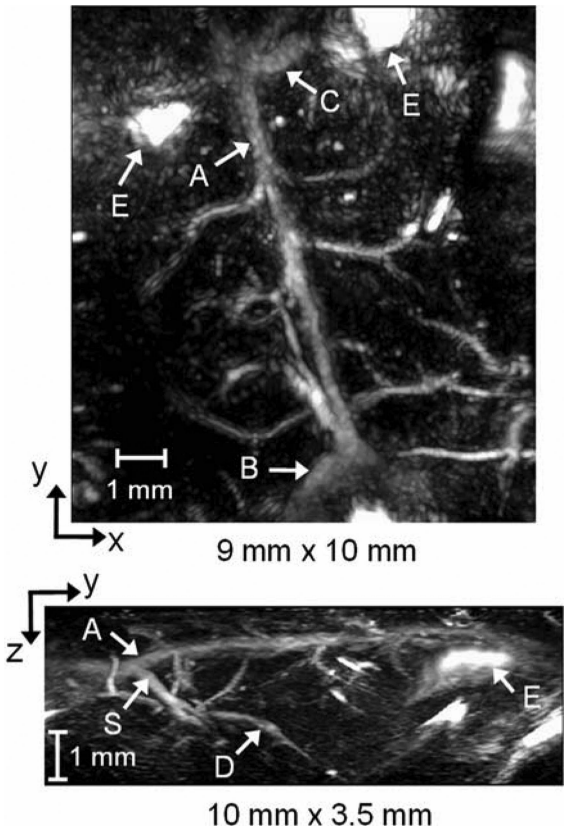

Fig. 4. Photoacoustic image of vasculature in mouse brain obtained using excitation wavelengths of 637 nm and 800 nm simultaneously. (top) x-y maximum intensity projection (MIP) of 3D photoacoustic image and (bottom) $y-z$ MIP. A, superior sagittal sinus B, transverse sinus; C—inferior cerebral vein; E, eyes; S, sinus rectus; D, inferior sagittal sinus.

150 μm so as not to exceed the maximum array size that the acquisition software could handle. The $x-y$, $x-z$, and $y-z$ MIPs are shown in Fig. 6 (Media 3). In

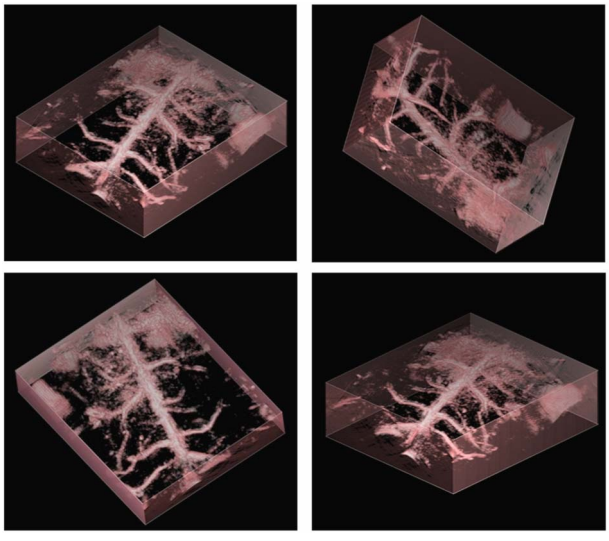

Fig. 5. (Color online) Volume rendered representation of images of mouse brain vasculature at different viewing angles obtained using excitation wavelengths of 637 nm and 800 nm simultaneously (Media 2). This image was reconstructed from the data set used to form the MIP images shown in Fig. 4.

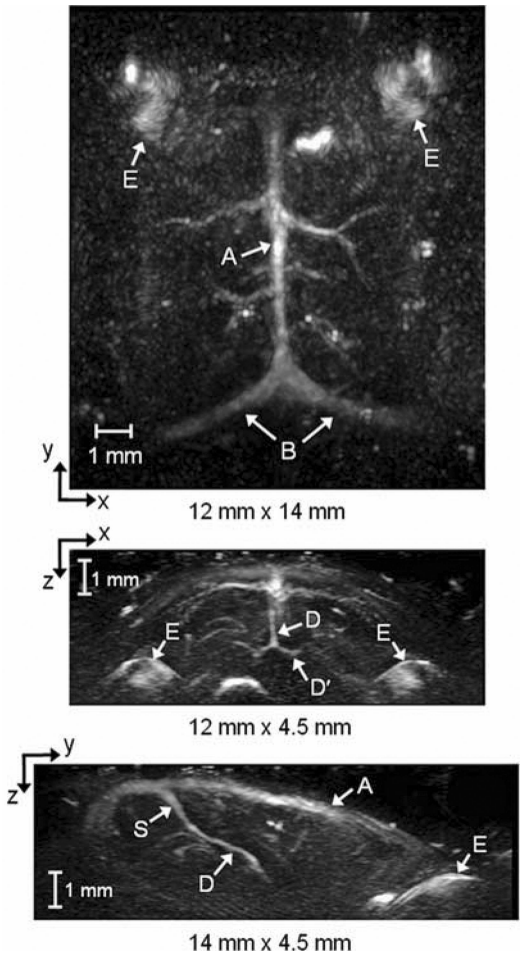

Fig. 6. Photoacoustic image of the vasculature in mouse brain obtained using an excitation wavelength of 889 nm (Media 3). (top) $x-y$ maximum intensity projection (MIP), (middle) $x-z$ MIP, and (bottom) $y-z$ MIP. A, superior sagittal sinus; B, transverse sinus; E, eyes; S, sinus rectus; D, inferior sagittal sinus; D′, lateral branching at the distal end of the inferior sagittal sinus.

common with the images shown in Figs. 2–5, the principal cerebral cortical vessels and the sagittal sinus and transverse sinus can be seen, albeit with reduced contrast. The sinus rectus and inferior sagittal sinus are also visible, but the latter can now be seen extending to a greater depth (~3.7 mm) than observed in Fig. 4. In addition, the branching of the inferior sagittal sinus at its distal end can be seen. This latter feature is most evident in the online animated volume rendered representation, which also reveals an earlier branching that is not discernible on the MIPs in Fig. 6 (Media 3).

4. Conclusion

The use of a novel photoacoustic imaging instrument for small animal brain imaging has been demonstrated. It has been shown that 3D images of the cerebral vascular anatomy can be obtained noninvasively through the intact skin and scalp to depths of several millimeters with high contrast and spatial resolution. It is noted that, as well as revealing

the superficial cortical vasculature, deeply lying features such as the inferior sagittal sinus and the branching at its distal end can be visualized. Such features have not generally been observed in previous photoacoustic imaging studies of the small animal brain [13–19].

There are several advantages of the system over other photoacoustic imaging instruments for imaging the small animal brain. These include the ease and convenience with which the instrument can be interfaced to the animal. This is a consequence of the transparent nature of the sensor head, which allows it to be placed on the surface of the head of the animal and the photoacoustic signals recorded over a planar surface coincident with the excitation light. It thus obviates the need for fully immersing the animal in acoustic couplant or the use of complex holders for the head, which schemes based on cylindrical detection geometries often require. The sensor also provides a level of acoustic performance that can be difficult to achieve with piezoelectric based detection methods, particularly in relation to the spatial sampling of the incident acoustic field as discussed in Ref. [23]. Because the sensor is optically addressed using a focused laser beam, the incident acoustic field can be spatially sampled with significantly higher (potentially optical diffraction limited) resolution than can be achieved with piezoelectric receivers. It is this along with the broadband uniform acoustic frequency response of the sensor and its high detection sensitivity that are responsible for the high contrast and spatial fidelity of the reconstructed images. Although the penetration depth is not currently as great as some photoacoustic imaging systems [20], there is, as noted in Ref. [23], significant potential to increase it by increasing detection sensitivity. In addition there is the prospect of increasing the sensor bandwidth and optimizing the spatial sampling parameters to obtain higher spatial resolution. While the current acquisition speed may be acceptable for studying slow long term structural changes such as the evolution of the vasculature of a tumor over a period of days it would be insufficient for studying more rapid events such as the hemodynamic response to functional activation in the brain, which may occur on a subsecond time scale. However, there is significant scope to increase acquisition speed, potentially obtaining real time image acquisition rates, especially if 2D images are acceptable, through the use of higher repetition rate laser systems [28,29] or parallelizing the sensor read-out scheme using a photodetector array as described in Ref. [30]. Finally, the optical nature of the sensor lends itself to multimodal imaging studies. For example, the system can readily be made compatible with MRI as the sensor head is fabricated from nonmagnetic materials and its transparent nature would allow fluorescence and bioluminescence emissions to be imaged through it.

In summary, this type of instrument may provide a useful tool that is complementary to other preclinical imaging techniques for characterizing small animal models of brain injury and disease processes, particularly those that require studying vascular anatomy and function such as stroke, epilepsy, and traumatic brain injury.

This work was supported by the UK Engineering and Physical Sciences Research Council.

References

1. M. F. Lythgoe, N. R. Sibson, and N. G. Harris, "Neuroimaging of animal models of brain disease," Br. Med. Bull. **65**, 235–257 (2003).
2. R. S. Balaban and V. A. Hampshire, "Challenges in small animal noninvasive imaging," ILAR J. **42**, 248–263 (2001).
3. E. Hillman, "Optical brain imaging in vivo: techniques and applications from animal to man," J Biomed. Opt. **12**, 051402 (2007).
4. L. Wang and H.-i. Wu, *Biomedical Optics: Principles and Imaging* (Wiley, 2007).
5. M. Cope, "The application of near infrared spectroscopy to noninvasive monitoring of cerebral oxygenation in the newborn infant," Ph.D. dissertation (University College London, 1991).
6. S. R. Cherry, "*In vivo* molecular and genomic imaging: new challenges for imaging physics," Phys. Med. Biol. **49**, R13–R48 (2004).
7. A. P. Gibson, J. C. Hebden, and S. R. Arridge, "Recent advances in diffuse optical imaging," Phys. Med. Biol. **50**, R1–R3 (2005).
8. J. G. Laufer, D. T. Delpy, C. E. Elwell, and P. C. Beard, "Quantitative spatially resolved measurement of tissue chromophore concentrations using photoacoustic spectroscopy: application to the measurement of blood oxygenation and hemoglobin concentration," Phys. Med. Biol. **52**, 141–168 (2007).
9. P. C. Beard, "Flow velocity measurements," UK patent application, WO 03/039364 (2001).
10. H. Fang, K. Maslov, and L. V. Wang, "Photoacoustic Doppler effect from flowing small light-absorbing particles," Phys. Rev. Lett. **99**, 184501 (2007).
11. A. De La Zerda, C. Zavaleta, S. Keren, S. Vaithilingam, S. Bodapati, Z. Liu, J. Levi, B. Smith, M. Te-Jen, O. Oralkan, Z. Cheng, X. Chen, H. Dai, B. Khuri-yakub, and S. Gambhir, "Carbon nanotubes as photoacoustic molecular imaging agents in living mice," Nat. Nanotechnol. **3**, 557–562 (2008).
12. M.-L. Li, J.-T. Oh, X. Xie, G. Ku, W. Wang, C. Li, G. Lungu, G. Stoica, and L. V. Wang, "Simultaneous molecular and hypoxia imaging of brain tumors in vivo using spectroscopic photoacoustic tomography," Proc. IEEE **96**, 481–489 (2008).
13. X. Wang, Y. Pang, G. Ku, X. Xie, G. Stoica, and L. V. Wang, "Noninvasive laser-induced photoacoustic tomography for structural and functional in vivo imaging of the brain," Nat. Biotechnol. **21**, 803–806 (2003).
14. X. Wang, G. Ku, M. A. Wegiel, D. J. Bornhop, G. Stoica, and L. V. Wang, "Noninvasive photoacoustic angiography of animal brains in vivo with near-infrared light and an optical contrast agent," Opt. Lett. **29**, 730–732 (2004).
15. S. Yang, D. Xing, Q. Zhou, L. Xiang, and Y. Lao, "Functional imaging of cerebrovascular activities in small animals using high-resolution photoacoustic tomography," Med. Phys. **34**, 3294–3301 (2007).
16. Q. Zhang, Z. Liu, P. Carney, Z. Yuan, H. Chen, S. Roper, and H. Jiang, "Non-invasive imaging of epileptic seizures in vivo using photoacoustic tomography," Phys. Med. Biol. **53**, 1921–1931 (2008).

17. K. H. Song, G. Stoica, and L. V. Wang, "In vivo three-dimensional photoacoustic tomography of a whole mouse head," Opt. Lett. **31**, 2453–2455 (2006).
18. R. A. Kruger, W. L. Kiser, Jr., D. R. Reinecke, G. A. Kruger, and K. D. Miller, "Thermoacoustic optical molecular imaging of small animals," Mol. Imaging **2**, 113–123 (2003).
19. X. Wang, Y. Pang, and G. Ku, "Three-dimensional laser-induced photoacoustic tomography of mouse brain with the skin and skull intact," Opt. Lett. **28**, 1739–1741 (2003).
20. J. Gamelin, A. Aguirre, A. Maurudis, F. Huang, F. Castillo, L. V. Wang, and Q. Zhu, "Curved array photoacoustic tomographic system for small animal imaging," J. Biomed. Opt. **13**, 024007 (2008).
21. L. V. Wang, "Tutorial on photoacoustic microscopy and computed tomography," IEEE J. Sel. Top. Quantum Electron. **14**, 171–179 (2008).
22. E. W. Stein, K. Maslov, and L. V. Wang, "Noninvasive mapping of the electrically stimulated mouse brain using photoacoustic microscopy," Proc. SPIE **6856**, 68561J (2008).
23. E. Zhang, J. Laufer, and P. C. Beard, "Backward-mode multiwavelength photoacoustic scanner using a planar Fabry Perot polymer film ultrasound sensor for high resolution three-dimensional imaging of biological tissues," Appl. Opt. **47**, 561–577 (2008).
24. K. Koestli, M. Frenz, H. Bebie, and H. Weber, "Temporal backward projection of optoacoustic pressure transients using Fourier transform methods," Phys. Med. Biol. **46**, 1863–1872 (2001).
25. E. Z. Zhang, J. Laufer, and P. C. Beard, "Three dimensional photoacoustic imaging of vascular anatomy in small animals using an optical detection system," Proc. SPIE **6437**, 643710S (2007).
26. British Standard BS EN 60825-1, "Safety of laser products. Equipment classification, requirements and user's guide," 1994.
27. http://www.medphys.ucl.ac.uk/research/mle/images.htm.
28. K. Maslov, H. F. Zhang, and L. V. Wang, "Portable real-time photoacoustic microscopy," Proc. SPIE **6437**, 643727 (2007).
29. T. J. Allen and P. C. Beard, "Pulsed NIR laser diode excitation system for biomedical photoacoustic imaging," Opt. Lett. **31**, 3462–3464 (2006).
30. M. Lamont and P. C. Beard, "2D imaging of ultrasound fields using a CCD array to detect the output of a Fabry Perot polymer film sensor," Electron. Lett. **42**, 187–189 (2006).